Autonomous microscopic bunch inspection using region-based deep learning for evaluating graphite powder dispersion

Hai Liu [a], Aimin Sha [a,*], Zheng Tong [a,*], Jie Gao [a,b,*]

[a] School of Highway, Chang'an University, Xi'an 710061, PR China
[b] Department of Civil Engineering, Liverpool John Moores University, Peter Jost Enterprise Centre, Byrom Street, L3 3AF Liverpool, United Kingdom

HIGHLIGHTS

- Project presents an application of convolutional neural networks (CNN) in evaluating graphite powder dispersion.
- Different Faster R-CNNs are established by the processes of structure design, training and testing.
- The optimal well-trained Faster R-CNN is able to locate graphite powder bunch with acceptable precision and high efficiency.
- The method based on the Faster R-CNN had the capacity of quasi real-time autonomous dispersion evaluation in GPU mode.

ARTICLE INFO

ABSTRACT

The ice-snow melting performance of ice-snow pavement is significantly influenced by the dispersion of graphite powder, particularly through the distribution of graphite powder bunches. In recent years, optical microscope (OP) images have been utilized to detect graphite powder bunches and evaluate their dispersion. However, because graphite powder bunches and other objects in OP images often have various shapes, and conventional manually processed images of tasks have the disadvantage of low efficiency, it is a challenge to detect graphite powder bunches and evaluate their dispersion using OP images. Therefore, this paper presents a novel application of a Faster Region Convolutional Neural Network (Faster R-CNN) using OP images and video sequences for the autonomous detection of graphite powder bunches and an evaluation of their dispersion. The research procedure is as follows: (a) generate a database for the Faster R-CNN, (b) design 30 Faster R-CNNs to find the optimal one, and (c) conduct an analysis of the training and testing results, along with new image testing, comparative studies, and video testing. The results show that a Faster R-CNN with nine anchors and a ratio of 0.3, 1.0, and 1.6, and with the sizes of 32, 128, and 192, has an average precision of the bunches and a dispersion uniformity of 91.2% and 84.0%, respectively. Its mean average precision is 87.5%. The Faster R-CNN is considered optimal in this research. The test time required to evaluate an image with a pixel resolution of 1024×1024 pixel in GPU mode is approximately 0.04 s, which means the method based on a Faster R-CNN has the capacity of a quasi-real-time autonomous dispersion evaluation in GPU mode to replace a human-assisted microscopic dispersion evaluation in OP images. The results also provide the possibility for a quasi-real-time evaluation using OP video sequences. Compared with a Fast R-CNN, a Faster R-CNN provides more reasonable bounding boxes for bunches and reliable results in terms of the dispersion uniformity.

© 2018 Elsevier Ltd. All rights reserved.

1. Introduction

A functional pavement has become an important part of pavement construction in China, including ice-snow melting pavements. The development of pavement materials that fit a functional pavement is a significant requirement. As a modifier of ice-snow melting pavements, graphite powder has been widely used in thermally and electrically conductive asphalt concrete [1,2]. Graphite powder has high thermal and electrical conductivity, obvious anisotropy, and porosity. Additionally, compared with other materials, such as carbon fiber, steel slag and copper slag [3], the large specific surface area and lubricating property of graphite powder make it easy to be uniformly dispersed in asphalt [4,5]. The dispersion of graphite powder uniformly in asphalt can form network channels in the interior of the asphalt mortar, which

* Corresponding authors at: School of Highway, Chang'an University, Xi'an 710061, PR China.
  E-mail addresses: tongzheng1992@outlook.com (Z. Tong), ams@chd.edu.cn (A. Sha), highway-gaojie@st.chd.edu.cn (J. Gao).

improves the ice-snow melting pavement properties, such as the temperature performance, fracture toughness, and electrical conductivity, as well as the optical absorption property and light-thermal conversion efficiency [6–8]. These improved properties have positive effects on the functional performance of thermally and electrically conductive asphalt concrete pavement. Clearly, the dispersion of graphite powder is an important factor for properties of ice-snow melting pavement. Therefore, it is important to develop methods to evaluate the dispersion of graphite powder in asphalt.

There are many methods used to evaluate the dispersion of modifiers, such as a digital image method, mathematical morphology measurement, and alternating current impedance spectroscopy (AC-IS). Kang et al. [9] quantitatively evaluated the dispersion of modified particles by extracting the characteristic parameters of the dispersed phase in microscopic images. Fang et al. [10] segmented a scanning electron microscope (SEM) photograph of rubber filled with carbon black (CB), and evaluated the dispersion of CB particles by acquiring the geometric characteristics of the particles based on the principle and method of mathematical morphology. Woo et al. [11] evaluated the dispersion of fiber based on the intrinsic electrical conductivity of the cement composites using AC-IS. Wang et al. [12] evaluated the cracking resistance of cement mortar and the dispersion of its modifiers using SEM. Compared with other evaluation methods, the microscopic digital image method has certain advantages: (1) visualization of the material morphostructure, and (2) the potential to be combined with advanced image processing techniques. In recent years, a dispersion evaluation using a microscopic digital image method has obtained certain achievements. Xiao et al. [13] continuously observed the dispersion of Styrene-Butadiene-Styrene (SBS) in asphalt during the mixing process using a fluorescence microscope (FM), and qualitatively analyzed the microscopic dispersion of SBS modified asphalt. Yao et al. [14] observed the dispersion state of a nanomaterial modified asphalt using an atomic force microscope (AFM), and analyzed the modified effects of three types of nanomaterial on the matrix asphalt. Gao et al. [15] captured microstructural images of carbon-fiber-reinforced cement-based composites (CFRC) using SEM, and analyzed the dispersion of carbon fiber in the concrete composites. Huang et al. [16] used a transmission electron microscope (TEM) to analyze the effects of the carbonization pressure on the microstructure of graphitized pitch-derived carbons. The results indicate that the dispersion and orientations of the sample prepared at 30 MPa are better than those of the sample prepared at 60 MPa. Shen et al. [17] measured the microstructure and dispersion of asphalt at different diffusion positions using AFM, and analyzed the diffusion mechanism of different types of regenerant. Wang et al. [18] determined the gray thresholds of different components in OP images, and analyzed the dispersion of carbon fiber. In summary, microscope methods play an important role in analyzing the dispersion of modifiers. Although the above methods can be used to evaluate the dispersion through the application of digital microscopic images, certain problems remain: (1) some human assistance is required to locate the bunches and evaluate the dispersion in digital microscopic images, (2) the stability of algorithms used to locate the bunches and evaluate the dispersion can be affected by the image quality, and (3) only static images can be analyzed. Therefore, the development of a graphite powder dispersion evaluation system based on static OP images and videos, which possess sufficient stability toward different real-world conditions, is a key research issue.

With the continuous development of deep learning techniques, first proposed by Lecun et al. [19,20], convolutional neural networks (CNNs) have demonstrated significant advantages in the field of object recognition [21,22] and property evaluation [23,24]. In recent years, CNNs have been successfully applied in civil engineering. For example, Tong et al. [23,25,26] employed CNNs to calculate the lengths of the pavement surface cracks and reflection cracks based on digital images and ground penetrating radar data, respectively. The results of these studies demonstrated that CNNs have stability against the influence of pavement materials and highway structures. Additionally, a CNN was utilized to recognize different subgrade defects based on ground penetrating radar images [27]. Cha et al. [28,29] detected pavement damage and visual structure defects using deep learning, and the results demonstrated that CNNs can be used to find visual defects in different structures in real-world situations. Lin et al. [30] detected structural damage using automatic feature extraction through deep learning. Liao et al. [31] presented a deep-learning method for a reduction in carbon emissions. Additionally, there have been some studies combining CNNs with images for damage detection during the past few years [32–35]. In general, two properties of a CNN, stability and automation during feature extraction, are considered attractive in the inspection of bunches and a dispersion evaluation system. Stability indicates a strong tolerance for translation and distortion when learning deep features from input images. Automation indicates the learning of deep features with no assistance from humans. These two properties are important for evaluation problems in a dispersion analysis when handling complex backgrounds and feature information in OP images. Therefore, it is reasonable to employ CNNs to construct the relationship between OP images and graphite powder dispersion based on the major factors introduced above.

In this study, we use Faster R-CNNs to locate graphite powder bunches in OP images and construct a relationship between OP images and graphite powder dispersion. The novelty of this study is that Faster R-CNNs can locate graphite powder bunches and evaluate the dispersion in OP images autonomously. Additionally, an optimal Faster R-CNN has acceptable stability, which is not affected by the lighting conditions. Compared with former research methods for evaluating the dispersion, we realized a method based on a Faster R-CNN with no human assistance and better algorithm stability. The rest of this article is organized as follows. In Section 2, the procedure for generating a database of OP images is explained followed by the description of the Faster R-CNN and training implementation in our research. In Section 3, the results of the training and validation processes, as well as testing, are discussed and compared with a conventional Fast R-CNN. In Section 4, the testing of an optimal Faster R-CNN on OP videos is presented to realize a continuous detection and dispersion evaluation of graphite powder bunches in asphalt.

2. Research approaches

2.1. Generation database for CNNs

2.1.1. Raw materials

(1) Asphalt

The asphalt used in this research was 90# petroleum asphalt for heavy traffic road pavement (AH-90#). The basic indexes and corresponding requirements are shown in Table 1.

(2) Graphite

The graphite powder used in this research was analytically pure DK graphite powder. The main physicochemical properties are given in Table 2.

Table 1
The basic indexes and requirements of AH-90#

Indexes		Results	Requirement
Penetration, 25 °C, 100 g, 5 s/(10^{-1} mm)		87.2	80–100
Ductility, 5 cm/min, 15 °C/(cm)		>125	≥100
Softening point (ring and ball method)/(°C)		45.0	≥42
Density (15 °C)/(g·cm^{-3})		1.03	–
Wax content (distillation method)/(%)		1.67	≤3.0
Flashing point (COC)/(°C)		278	≥245
Solubility (trichloroethylene)/(%)		99.7	≥99.5
Residuum properties of film oven after aging	Mass loss/(%)	−0.04	≤ ±0.8
	Residual penetration ratio, 25 °C, 100 g, 5 s/(%)	72	≥54
	Residual ductility, 5 cm/min, 15 °C/(cm)	>100	≥20

2.1.2. Sample preparation

The dispersion of graphite powder in asphalt mortar depends on the preparation technologies and methods. An FM300 high-speed shear apparatus was used to prepare the asphalt mortar. Asphalt mortar contains 400 g of asphalt and 73.7 g of graphite powder, the latter of which accounts for 8% of the asphalt volume. The dispersion of graphite powder in asphalt mortar was influenced by the shearing temperature, time, and revolving speed [36–38]. To acquire asphalt mortar with a different dispersion of graphite powder, an orthogonal test, including the different temperatures, shearing time, and revolving speed, was conducted [39]. The detailed information of the orthogonal test is given in Table 3.

2.1.3. OP images

The analytical method based on microscopic morphostructure was an effective way to research the dispersion of modified asphalt [40,41]. The quality of microscopic images captured by OP has a close relationship with the preparation conditions of the samples. The conditions including the bottom temperature of the microscope slides, the temperature of the hot asphalt drops, the sizes of the droplets, and the pressure of the cover glasses influenced the preparation of the samples and sequentially influenced the image quality. To prepare proper samples and capture high-resolution microscopic images, the naturally flowing film method [42] was used to prepare the observed samples.

Step 1. A microscope slide suspended above the electric furnace was heated.

Step 2. Hot asphalt was dipped onto the slide with a fine glass rod, and a cover glass was placed on the slide until the hot asphalt naturally flowed and formed a film under the high temperature.

Step 3. The sample was observed using OP after the temperature of the slide was close to the indoor temperature.

According to the observation method above, the storage time of the sample observed was 8–12 h, and the main observation range was as shown in Fig. 1(g), where the red rectangles indicate approximately the observation range of each observed dot in each sample. A part of a microscopically observed sample is shown in Fig. 1(a). The OP used in this research was a LW300LFT (LED) fluorescence optical microscope connected with a microscopic digital camera. The amplification of the objective lens in the microscope was ×10, which eliminated any chromatic aberrations with a 0.35 numerical aperture. The total amplification was ×100. Additionally, a transmission light source was used for the observation. A live observation image is shown in Fig. 1(b). As shown in Fig. 1(c) through (f), the components of the graphite modified asphalt mortar could be generally distinguished under the OP. Therefore, the dispersion of graphite powder in asphalt mortar can be observed using this method. Microscopically observed images at a pixel resolution of 2048 × 2048 are also shown in Fig. 1(c) through (f). In these images, bunches in the black area are graphite powder, the

Table 2
Main properties of graphite powder.

Density/(g·cm^{-3})	Mohs Hardness	Particle diameter/(μm)	Carbon content/(%)	
2.372	1–2	150	98.9	
Ash content/(%)	Ferric content/(%)	Thermal conductivity/W·(m·°C)$^{-1}$	Electric conductivity/Ω·cm	
0.2	0.03	68–72	3.0×10^5	

Table 3
Orthogonal test schedule.

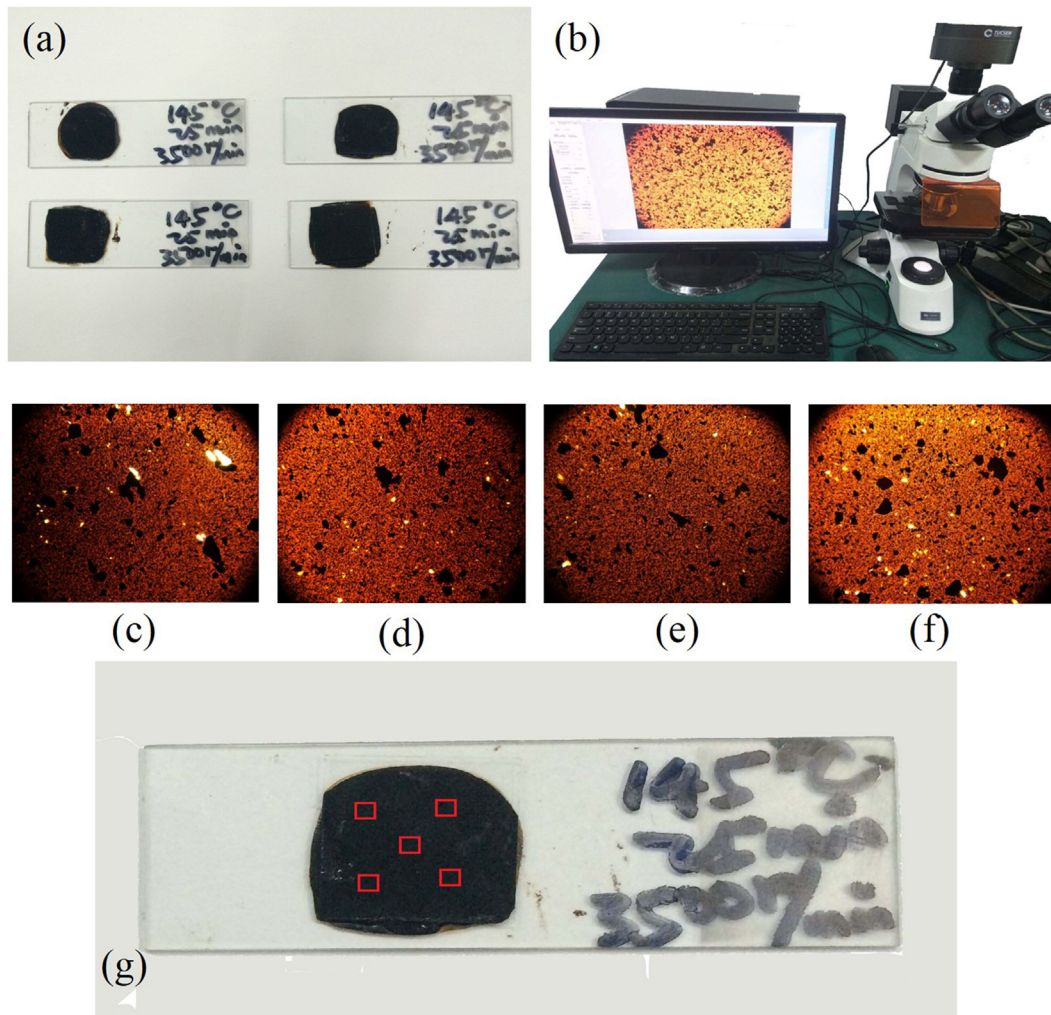| Serial number	Temperature/(°C)	Time/(min)	Revolving speed/(r·min^{-1})	High-speed shear apparatus of modified asphalt
1	135	20	2000	
2	135	25	2500	
3	135	30	3000	
4	135	35	3500	
5	140	20	2500	
6	140	25	2000	
7	140	30	3500	
8	140	35	3000	
9	145	20	3000	
10	145	25	3500	
11	145	30	2000	
12	145	35	2500	
13	150	20	3500	
14	150	25	3000	
15	150	30	2500	
16	150	35	2000	

Fig. 1. Microscopic observation of samples and images ($\times 100$).

dispersed black dots are uniformly dispersed graphite powder in asphalt, the white bright spots are transmitted light spots, and the yellow parts are asphalt.

2.2. Convolutional neural network

To locate graphite powder bunches in OP images and evaluate graphite powder dispersion in asphalt, the Faster R-CNN method was used for the real-time processing of images and videos. The original Faster R-CNN was composed of a region proposal network (RPN) to provide graphite powder bunch proposals in images, and Fast R-CNN to locate graphite powder bunch proposals provided by the RPN and to evaluate graphite powder dispersion in OP images. The details of the Faster R-CNN in our research are explained in this section, including the fundamental theories of a CNN, the description of a Fast R-CNN and an RPN, and the realization of the Faster R-CNN by sharing a CNN between an RPN and a Fast R-CNN.

2.2.1. Fundamental theories

In this section, the fundamental theories and concepts of the CNN are presented briefly, mainly including a convolutional layer, pooling layer, fully connected layer, softmax layer, and regression layer. Detailed information of these structural layers can be found in research studies conducted by Tong et al. [24] and Cha et al. [29].

(1) Convolutional layer. The main function of a convolutional layer in a CNN, which includes a set of kernels with learnable weights, is to compute object features through a convolution operation. Kernels have the same depth as the input of their layer, but a smaller width and height. For the image convolution, each kernel slides in the image from the left-upper corner to the lower-right corner. As a result, the image can be divided into several overlapping sub-windows to extract features from images. A set of kernels can extract different features from images.

(2) Pooling layer. The main function of a pooling layer (whether max or mean pooling) is to decrease the spatial size of its input, which reduces the computational costs and probability of overfitting. A max pooling layer slides a window on the input and outputs the maximum value from its respective field, whereas a mean pooling layer slides a window on the input and outputs the average value from its respective field.

(3) Fully connected layer. As a conventional layer in a neural network, a fully connected layer connects all neurons in its previous layer. The main function of the layer is to create a dot product and add a bias to its inputs in each neuron.

(4) Softmax layer. A softmax layer is the most common classifier utilized in a CNN, whose main function is to predict the class of its input. In general, the layer analyzes features from a

fully connected layer, computes the possibilities of each individual class, and shows the class with the highest probability as the classification results.

(5) Regression layer. There are two main functions of a regression layer in our research. First, a regression layer analyzes the features from a fully connected layer and computes the coordinates of graphite powder bunches in OP images. Second, a regression layer is used to evaluate graphite powder dispersion based on the numbers of bunches, and shows the results calculated by a softmax layer.
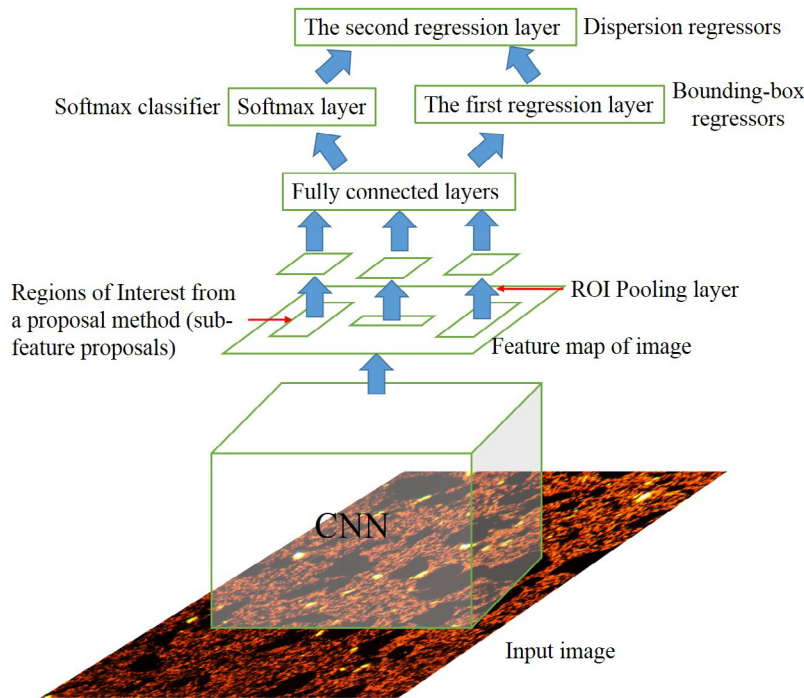
2.2.2. Fast R-CNN

A flow chart of a Fast R-CNN is shown in Fig. 2 and Table 4. The flow chart of the conventional CNN is also shown in Fig. 2. Compared with a conventional CNN, a Fast R-CNN has two specific layers called the Region of Interest (ROI) layer and ROI pooling layer. The two specific layers make the Fast R-CNN possible to locate specific objects, whereas a conventional CNN can only recognize objects in images but cannot locate them. The function of an ROI layer was to produce sub-feature proposals from feature maps from a convolutional neural network. The function of an ROI pooling layer was to take sub-feature proposals and apply a max pooling operation to extract a fixed-size feature vector from each sub-feature proposal. Fixed-size feature vectors were imported into fully connected layers, followed by a softmax layer and two regression layers, which were used to classify different components in OP images, calculate the locations of the bunches, and evaluate the graphite powder dispersion.

For each sub-feature proposal, the outputs of the softmax layer were the probability ($P = (P_0, P_1, P_2)$) of three classes, namely, graphite powder bunches, light-spots, and the background. The outputs of the first regression layer were four parameters representing the center coordinates (x, y), as well as the height and width (h, w) of the object. The outputs of the second regression layer were the evaluation results of dispersion in the OP image based on the outputs of the softmax layer and the first regression layer.

The training strategy of the Fast R-CNN was the mini-batch gradient descent. Referring to similar researches by Cha et al. [28] and Girshick [43], two images per iteration and 128 sub-feature proposals as mini-batches (25% positive and 75% negative) for each image were randomly selected to train the Fast R-CNN. Eq. (1) shows the loss function of the mini-batch gradient descent, where u and v are the label and coordinates of the bounding box of each truth value, respectively. In addition, $v = (x, y, h, w)$, u is 1 or zero for a positive or background ROI, and d is the dispersion uniformity within the range of 1 to zero. Eqs. (2), (3), and (4) show L_{cls}, L_{reg1}, and L_{reg2}, where X_1 and X_2 are the predicted value and ground truth value in different parts of the loss function.

$$Loss(P\ u\ T^u\ v\ D\ d) = L_{cls}(P\ u) + [u \geqslant 1] \sum_{i \in (x\ y\ h\ w)} L_{reg1}(T_i^u\ v_i) + L_{reg2}(D\ d) \quad (1)$$

$$L_{cls} = \frac{1}{1 + e^{-|X_1 - X_2|}} \quad (2)$$

(a) Flow chart of the Fast R-CNN
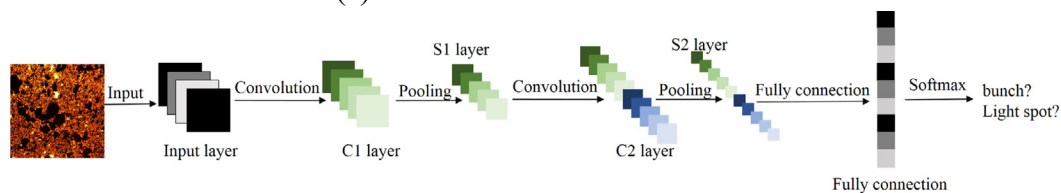
(b) Flow chart of conventional CNN

Fig. 2. Flow chart of Fast R-CNN and conventional CNN.

Table 4
Detailed specifications of Fast R-CNN.

Layer	Operator	Input Size	Filter size	Number	Stride
Input	–	$1024 \times 1024 \times 3$	–	–	–
L1	C1	$1024 \times 1024 \times 3$	$20 \times 20 \times 3$	96	2
L2	P1	$503 \times 503 \times 96$	7×7	–	2
L3	C2	$249 \times 249 \times 96$	$15 \times 15 \times 24$	192	2
L4	P2	$118 \times 118 \times 192$	4×4	–	2
L5	C3	$58 \times 58 \times 192$	$4 \times 4 \times 192$	384	1
L6	C4	$55 \times 55 \times 384$	$4 \times 4 \times 384$	384	1
L7	ROI Pooling	384	–	–	–
L8	FC + ReLU	4096	–	–	–
L9	Dropout	–	–	–	–
L10	FC + ReLU	4096	–	–	–
L11	Dropout	–	–	–	–
L12	FC + ReLU	3	–	–	–
L13	Softmax + Regressor				

Note: C = convolution operation; P = pooling operation; FC = fully connect; ReLU = rectified linear unit.

$$L_{reg1} = \begin{cases} 0.5(X_1 - X_2) & when |X_1 - X_2| \leqslant 1 \\ |X_1 - X_2| - 0.5 & when |X_1 - X_2| \succ 1 \end{cases} \quad (3)$$

$$L_{reg2} = \frac{1}{2N} \sum_{i=1}^{N} \|X_1 - X_2\|_2^2 \quad (4)$$

$$ReLU = \begin{cases} x & x \succ 0 \\ 0 & x \leqslant 0 \end{cases} \quad (5)$$

2.2.3. Region proposal network

As mentioned above, and shown in Fig. 2, a proposal method should be used to produce sub-feature proposals from feature maps in the ROI layer. In a Fast R-CNN, the 128 sub-feature proposals from two images per iteration as mini-batches were selected randomly, which leads to many meaningless computations and wastes a significant amount of time for the training and testing. Therefore, a region proposal network, as the proposal method in the ROI layer, was used to produce sub-feature proposals from the feature maps in our research. The architecture of the RPN is shown in Fig. 3 and Table 5. The inputs of the RPN are OP images and the outputs are a set of rectangular object proposals, including the probability of being a bunch or light-spot in each proposal. As shown in Fig. 3 and Table 5, the work processes of the RPN include two steps.

Step 1. Use a CNN to extract a feature map for each OP image. In Fig. 3, the feature maps are outputs of the last layer of the CNN. Notably, all the convolutional layers of the RPN in our research are followed by a ReLU as an activation function to increase the speed of convergence, which refers to work by Nair and Hinton [44]. ReLU is presented in Eq. (5).

Step 2. Feed a part of the feature maps to the regression and softmax layers. A part of a feature map, called the possible sub-feature proposals, as indicated in the red square in Fig. 3, is produced by a sliding window. The functions of the regression and softmax layers are predicting the coordinates of the multiple bounding boxes and the probability of being an object in each box, respectively.

As shown in Fig. 3, the key work of the RPN is to produce feature maps to generate object proposals as sub-feature proposals in the Fast R-CNN. In the RPN, there are nine rectangular boxes called anchors with three different widths and heights in the possible sub-feature proposals. Each anchor was expressed as (x_i, y_i, w_i^k, h_i^k), $k = 1, 2, 3$, where x_i and y_i were the center of the possible sub-feature proposals, and w_i^k, h_i^k were the width and height of the anchor. As for the number of anchors, we referred to the work of Cha et al. [28]. The intersection-over-union (*IOU*) was used to compute the overlap between an anchor and a ground truth. The *IOU* was calculated using Eq. (6). An anchor was labeled as positive if its *IOU* is higher than 0.7 [45] and was the highest among the nine anchors. The other eight anchors were thus not used for the training process of the RNP. The condition in which each *IOU* of a possible sub-feature proposal was lower than 0.3 was regarded as the background [45]. As for the detailed size and ratio of anchors used in this research, 15 combinations of seven different ratios (0.3, 0.4, 0.7, 1.0, 1.3, 1.6, and 1.9) and two combinations of sizes from six possible anchor sizes (32, 64, 96, 128, 192, and 256) were
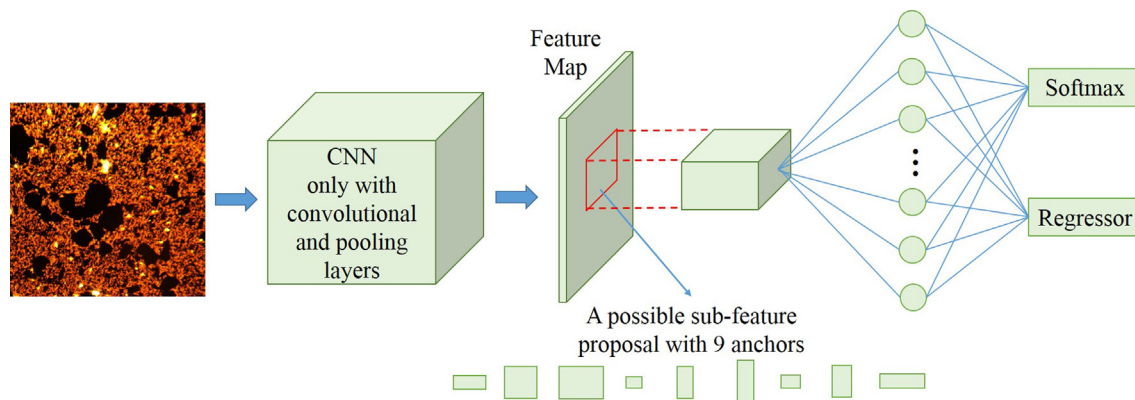

Fig. 3. Architecture of the RPN.

Table 5
Detailed specifications of the RPN.

Layer	Operator	Input Size	Filter size	Number	Stride
Input	–	$1024 \times 1024 \times 3$	–	–	–
L1	C1	$1024 \times 1024 \times 3$	$20 \times 20 \times 3$	96	2
L2	P1	$503 \times 503 \times 96$	7×7	–	2
L3	C2	$249 \times 249 \times 96$	$15 \times 15 \times 24$	192	2
L4	P2	$118 \times 118 \times 192$	4×4	–	2
L5	C3	$58 \times 58 \times 192$	$4 \times 4 \times 192$	384	1
L6	C4	$55 \times 55 \times 384$	$4 \times 4 \times 384$	384	1
L7	Sliding C1	$52 \times 52 \times 384$	$6 \times 6 \times 384$	256	2
L8	Sliding C2	$24 \times 24 \times 256$	$24 \times 24 \times 256$	–	1
L10	FC	256	–	–	–
L11	Softmax + Regressor				

Note: C = convolution operation; P = pooling operation; FC = fully connect.
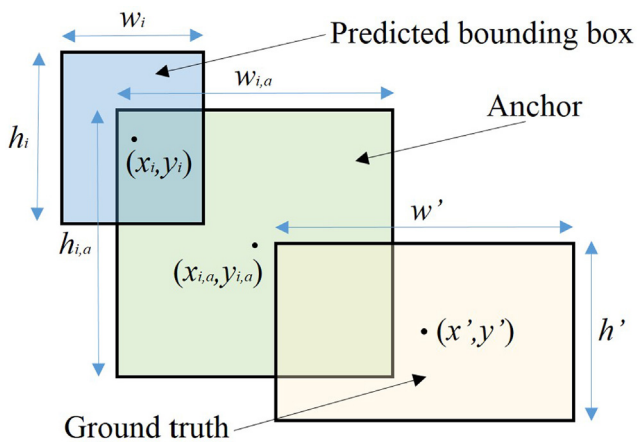

Fig. 4. A sketch map of the process used to calculate the loss function.

utilized to find the optimal anchor sizes and ratios because there were no proper researches to reference. Then, the possible sub-feature proposal with nine anchors was fed into a fully connected layer, followed by a softmax layer and a regression layer, to com-

pute the probability of objects from zero to 1, and predict the center coordinates, width, and height of a bounding box.

As for the training strategy of an RPN, the end-to-end mini-batch gradient descent with one image per iteration by randomly selecting 128 mini-batches was utilized. The loss function of the end-to-end mini-batch gradient descent is shown in Eq. (7), where i is a parameter with the relationship with the number of anchors, p_i and p_i' are the ground true label and predicted probability of being a bunch, light-spot, or background in each anchor, respectively. The functions of $m_{i,j}$ and $m_{i,j}'$ are to calculate the differences between the predicted bounding box and the anchor using Eq. (8), where (x_i, y_i), $(x_{i,a}, y_{i,a})$, and (x', y') are the predicted center coordinates of the bounding box by the ith anchor, i^{th} anchor, and ground truth with the highest IOU with the ith anchor, respectively, whereas (w_i, h_i), $(w_{i,a}, h_{i,a})$, and (w', h') are the width and height of the predicted bounding box, the ith anchor, and the ground truth with the highest IOU with the ith anchor, respectively. A sketch map of the process used to calculate the loss function through Eqs. (7) and (8) is shown in Fig. 4. By the end-to-end mini-batch gradient descent, the overlap between the predicted bounding box and the ground truth box was improved.

$$IOU = \frac{DetectionResult \cap GroundTruth}{DetectionResult \cup GroundTruth} \tag{6}$$
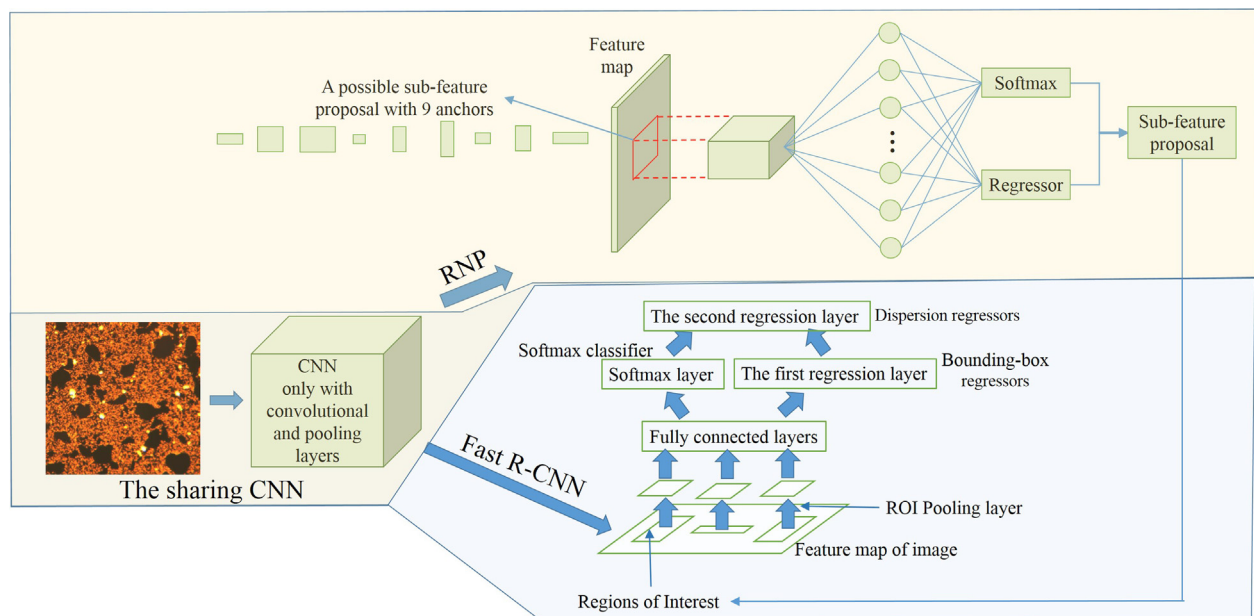

Fig. 5. Architecture of the Faster R-CNN.

$$Loss(p_i\ p_i'\ m_{i,j}\ m_{i,j}') = \frac{1}{N_{cls}} \sum_i L_{cls}(p_i\ p_i')$$
$$+ \frac{1}{N_{reg}} \sum_{j \in (x\ y\ w\ h)} p_i' L_{reg}(m_{i,j}\ m_{i,j}') \tag{7}$$

$$\begin{bmatrix} m_{i,x} & m_{i,y} \\ m_{i,w} & m_{i,h} \\ m_{i,x}' & m_{i,j}' \\ m_{i,w}' & m_{i,h}' \end{bmatrix} = \begin{bmatrix} (x_i - x_{i,a})/w_{i,a} & (y_i - y_{i,a})/h_{i,a} \\ \log(w_i/w_{i,a}) & \log(h_i/h_{i,a}) \\ (x' - x_{i,a})/w_{i,a} & (y' - y_{i,a})/h_{i,a} \\ \log(w'/w_{i,a}) & \log(h'/h_{i,a}) \end{bmatrix} \tag{8}$$

2.2.4. Faster R-CNN by sharing CNN between RPN and fast R-CNN

In the Faster R-CNN, we combined the RPN with a Fast R-CNN by sharing a CNN, as shown in Fig. 5. As can be seen from Fig. 4, Table 4, and Table 5, the first six layers of both the RPN and Fast R-CNN have the same specifications, and their weights and other computations can be shared, which can save time in training and testing. Four steps were applied to fine tune the parameters of the RPN and the Fast R-CNN to form the Faster R-CNN.

Step 1. The RNP was trained with random initial weights. In this step, the training targets were the object proposals of the Fast R-CNN, including graphite powder bunches and light-spots.

Step 2. The training weights of the Fast R-CNN were gained from the trained weights of the RNP in Step 1.

Step 3. The RPN was initialized with the final weights of the previous step and trained again.

Step 4. The object proposals, which were generated in Step 3, were used to train the Fast R-CNN with the initial parameters trained in step 3.

2.3. Database and implementation details

A database including 640 OP images (with a pixel resolution of 2048 × 2048) were collected by the method introduced in Section 2.1.3. The images were taken under different conditions (e.g., different lighting conditions and graphite powder dispersion), and the images were taken from 64 microscope slides. These images were cropped to 1024 pixels × 1024 pixels, and 2560 cropped images were acquired to generate the database for the Faster R-CNN. The labels and bounding box coordinates of the
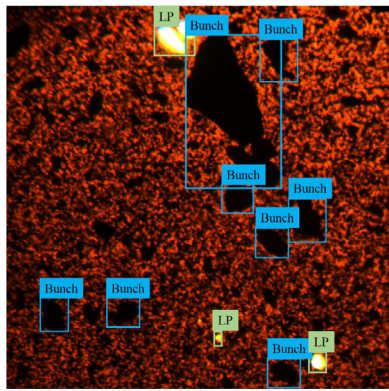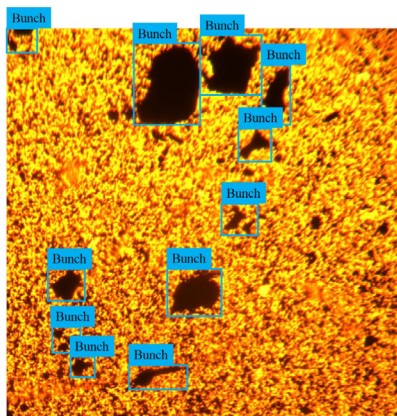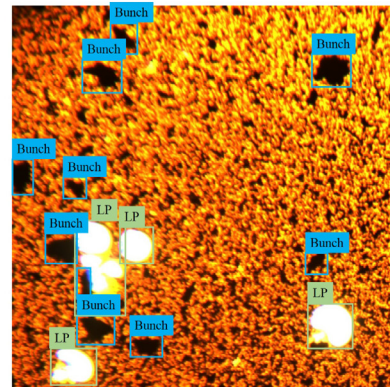

Dispersion uniformity: 11.00%

CEI: 10.1 mm
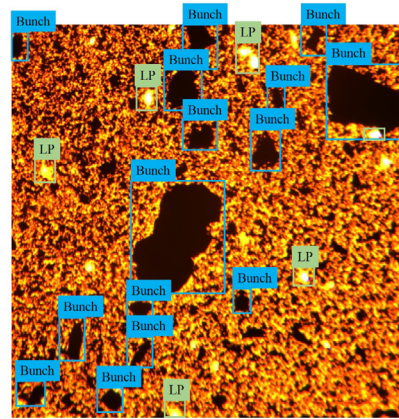
Dispersion uniformity: 12.91%

CEI: 12.0 mm

Dispersion uniformity: 8.68%

CEI: 8.6 mm

Dispersion uniformity: 4.12%

CEI: 7.9 mm

Fig. 6. Sample images with bounding boxes and labels (LP is the label for lighting spots).

objects were manually annotated in a Python environment. Some labels and bounding boxes during the annotation process are shown in Fig. 6. The standards for classifying the lighting spots, graphite powder bunches, and background are shown in [18], and the standards for a quantitative evaluation of dispersion are shown in Eq. (9), where $D_{effective}$ is the dispersion uniformity of graphite powder, which is a typical index used to evaluate the modifier dispersion in asphalt. In addition, A_{bu}, A_l, and A_{ba} are the areas of graphite powder bunches, lighting spots, and background in an OP image.

$$D_{effective} = \frac{A_{bu}}{A_{bu} + A_l + A_{ba}} \tag{9}$$

Additionally, the Clark-Evans nearest neighbor method [46] was also utilized to evaluate the dispersion uniformity. The distance between the nearest neighbor bunches was used to evaluate the dispersion uniformity in an OP image, which is called the Clark-Evans index (CEI). As mentioned above, all bunches were located using bounding boxes. Thus, the CEI of the bunches was equal to the minimum distance of the center coordinates of the bounding boxes in an OP image. According to the definition, with the increment in the CEI, the modified asphalt showed a good dispersion uniformity. Notably, the CEI from an OP image was one-hundred times smaller as the truth value when the total amplification applied was ×100.
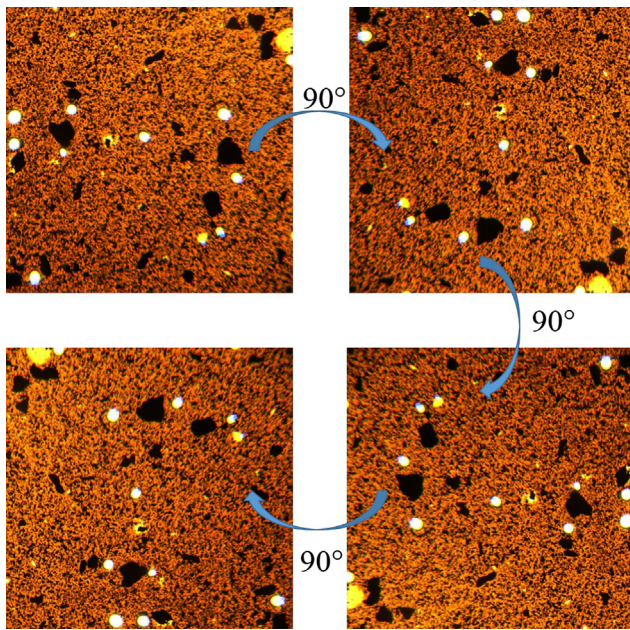

Fig. 7. Rotation operation for data augmentation.

To test the Faster R-CNN precisely, a test dataset was selected randomly from the 2560 cropped images with a pixel resolution of 1024 × 1024. The selected testing set contained 768 images, which were 30% of the total number. The remaining images were used to generate a training and validation dataset. Considering the method by He et al. [47] to realize a data augmentation, which reduces the probability of overfitting and improves the performance of a Faster R-CNN, a rotation operation was applied to the training and validation set, as shown in Fig. 7.

All experiments were conducted in a Python environment on a computer with a Core i7 6800 K @ 3.4 GHz CPU, 32 GB of DDR4 memory, and a12 GB NVIDIA Titan X GPU. The layers of the CNN and FC layers were initialized by zero. The RPN and Fast R-CNN networks were trained with a learning rate of 0.002, momentum of 1.0, and weight decay of 0.0010 for 60,000 and 30,000 iterations, respectively.

3. Results and discussion

3.1. Training, validation, and test results

During the training, the four-step strategy mentioned in Section 2.2.4 was conducted for 30 cases, which was designed to find the optimal anchor sizes and ratios, as mentioned in Section 2.2.4, and its precision was evaluated based on the performance of the testing set based on the average precisions of two objects, respectively, and mean average precision [28]. The mean average precision in this research was the mean value of the average precisions of the bunches, lighting spots, and dispersion uniformities. The average precisions of the two objects and mean average precision are shown in Fig. 8. As shown in Fig. 8, the highest average precision of the bunches is 92.4% in Case 5, whereas the average precision of the dispersion uniformity and mean average precision are 81.3% and 86.4%, respectively. However, the average precision of the dispersion uniformity and mean average precision are 84.0% and 87.5%, respectively, in Case 16, although its average precision of bunches is 91.2%, which is lower than that in Case 5. To create balance among the average precision of the bunches, the lighting points, the dispersion uniformity, and the mean average precision, Case 16 was considered as optimal, with ratios of 0.3, 1.0, and 1.6 and sizes of 32, 128, and 192.

3.2. Testing new images

To further test the performance of the Faster R-CNN in Case 16, 16 new OP images with a pixel resolution of 2048 × 2048 with different dispersion uniformities and lighting conditions, as shown in Table 3, were acquired using the method introduced in Section 2.1.2. Each image was cropped into four images with a pixel resolution of 1024 × 1024 and imported into the Faster
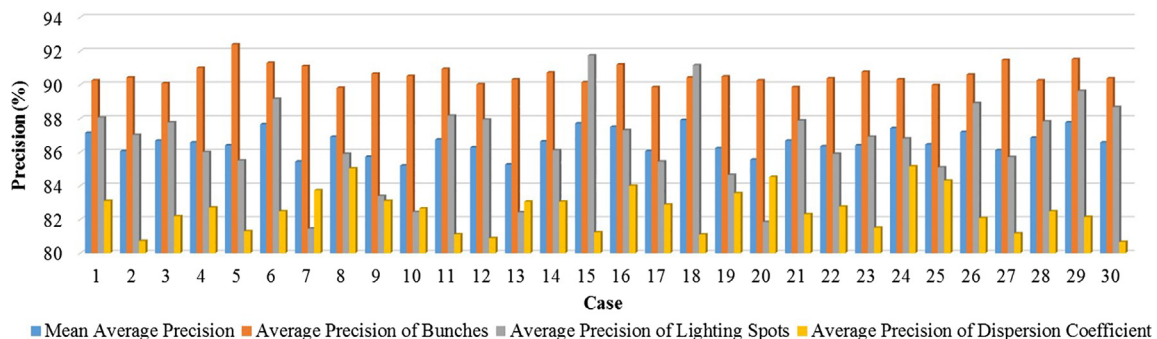

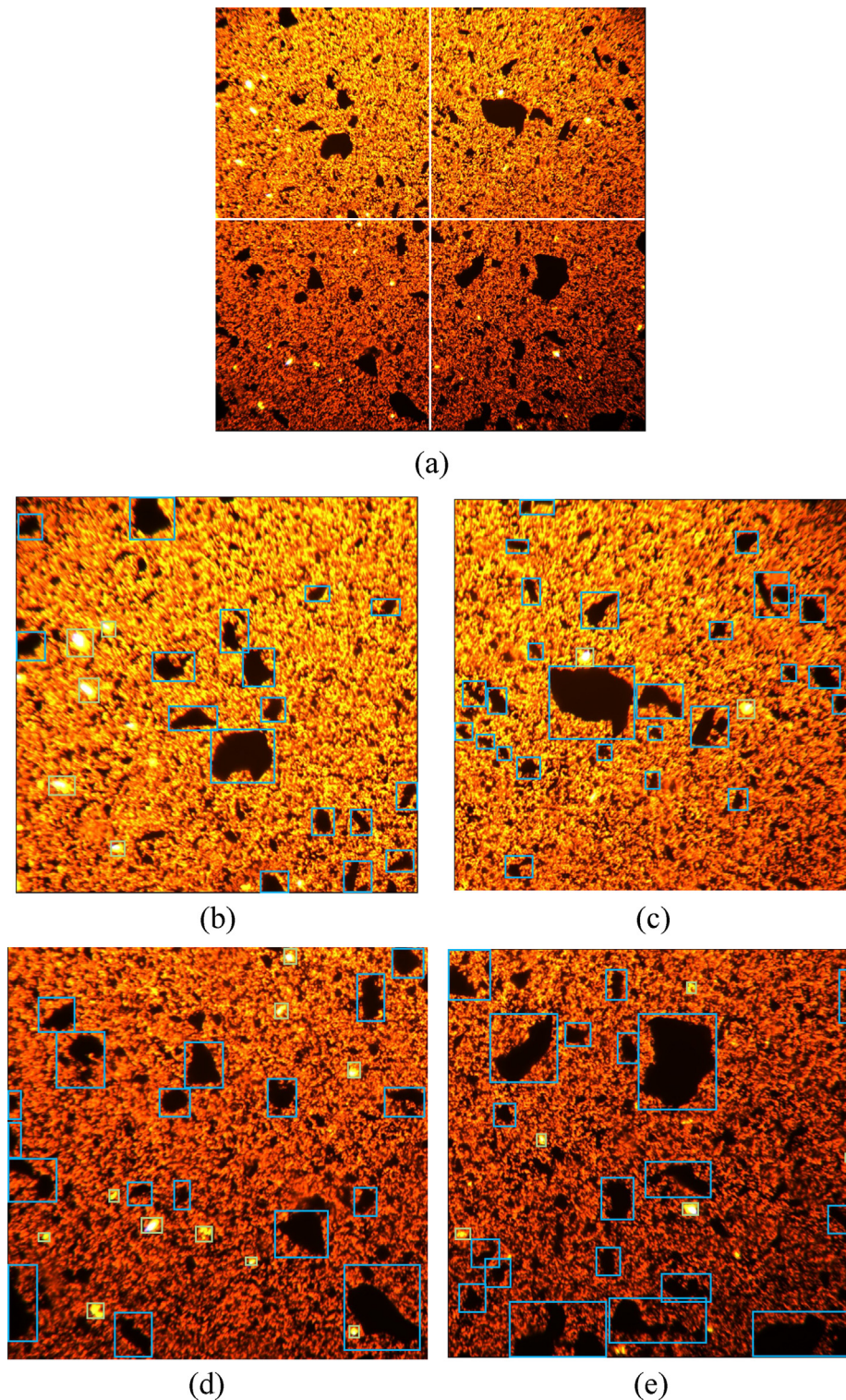**Fig. 8.** Test performance of Faster R-CNNs in different cases.

Fig. 9. An example of outputs of the Faster R-CNN under proper lighting conditions.

R-CNN in Case 16 to test the precision. The results of the outputs showed a mean average precision of 88.4% and average precisions of the bunches, lighting points, and dispersion uniformity of 92.4%, 89.4%, and 83.4%, respectively, which are similar to the test results described in Section 3.1. Therefore, we concluded that a Faster R-CNN can ensure a similar precision under real-world conditions. Two of the sixteen new OP images and their outputs are shown in Figs. 9 and 10.

Fig. 9 shows an OP image under proper lighting conditions and its outputs. We found that all the bunches and light spots were located by the Faster R-CNN, which were reasonable outputs of the Faster R-CNN. The reason why the Faster R-CNN could locate bunches and light spots was mainly owing to a set of kernels in convolutional layers. As mentioned above, the kernels in L1 extracted low-level features of bunches and light spots based on their different weight matrix, such as a part of the profile curves
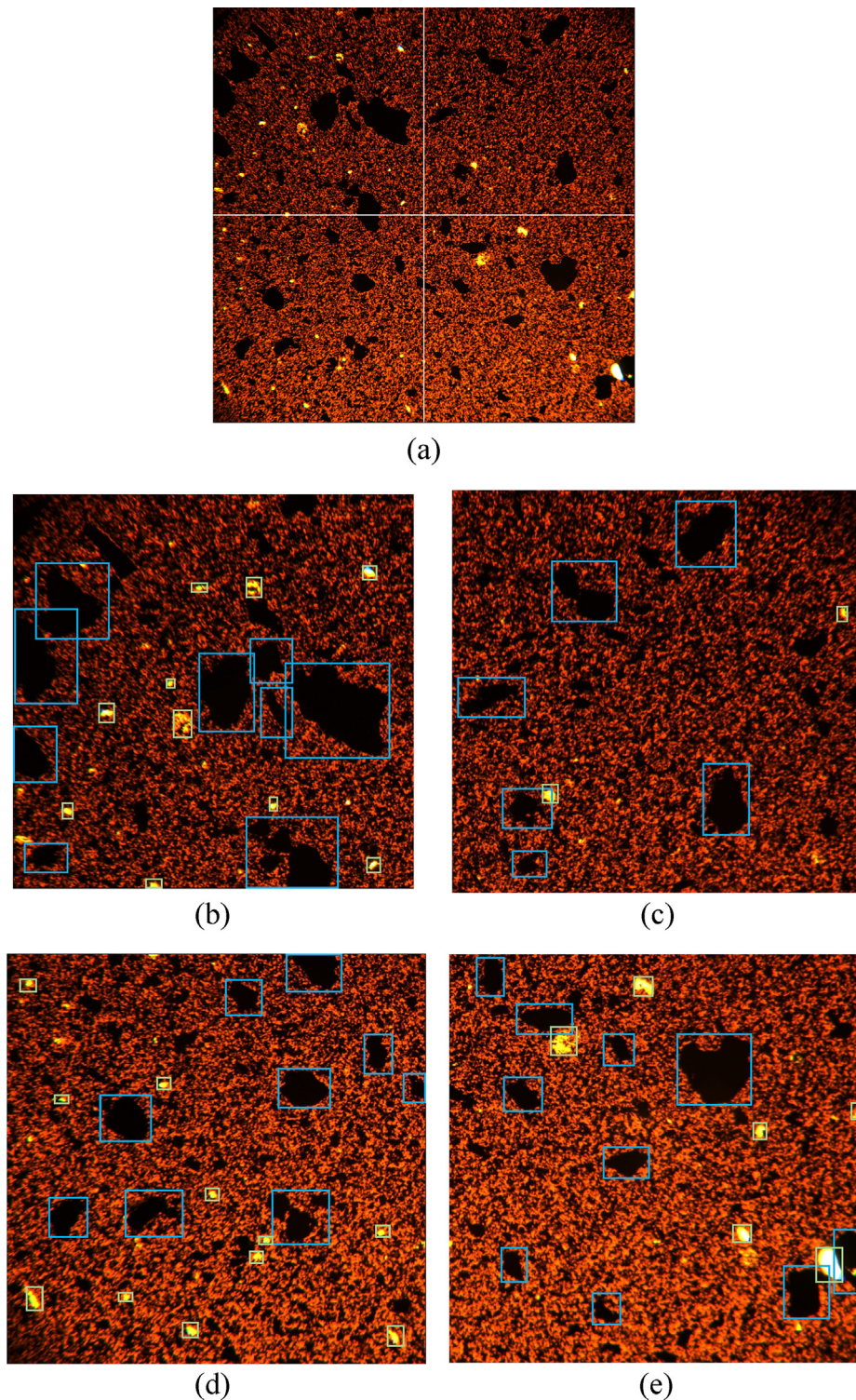
Fig. 10. An example of outputs of the Faster R-CNN under poor lighting conditions.

with a random shape and color information. For example, 96 kernels in L1 can extract 96 random shapes and color information features. Kernels in other convolutional layers can assemble high-level features based on low-level features, such as bunches with a random shape and specific colors in an RGB (red, green, blue) color space. A softmax layer and regression layer can classify and calculate the coordinates based on high-level features. Notably, there are several incomplete bunches shown in Fig. 10, which

may influence the evolution of dispersion uniformity. The problem can be solved through a continuous inspection using an OP video. Therefore, it is necessary to apply the Faster R-CNN in Case 16, not only in OP images but also in OP videos.

Fig. 10 shows an OP image in poor lighting conditions and its outputs. In general, the Faster R-CNN could locate bunches under poor lighting conditions, the reason for which is mainly from different kernels with a different weight matrix extracting different
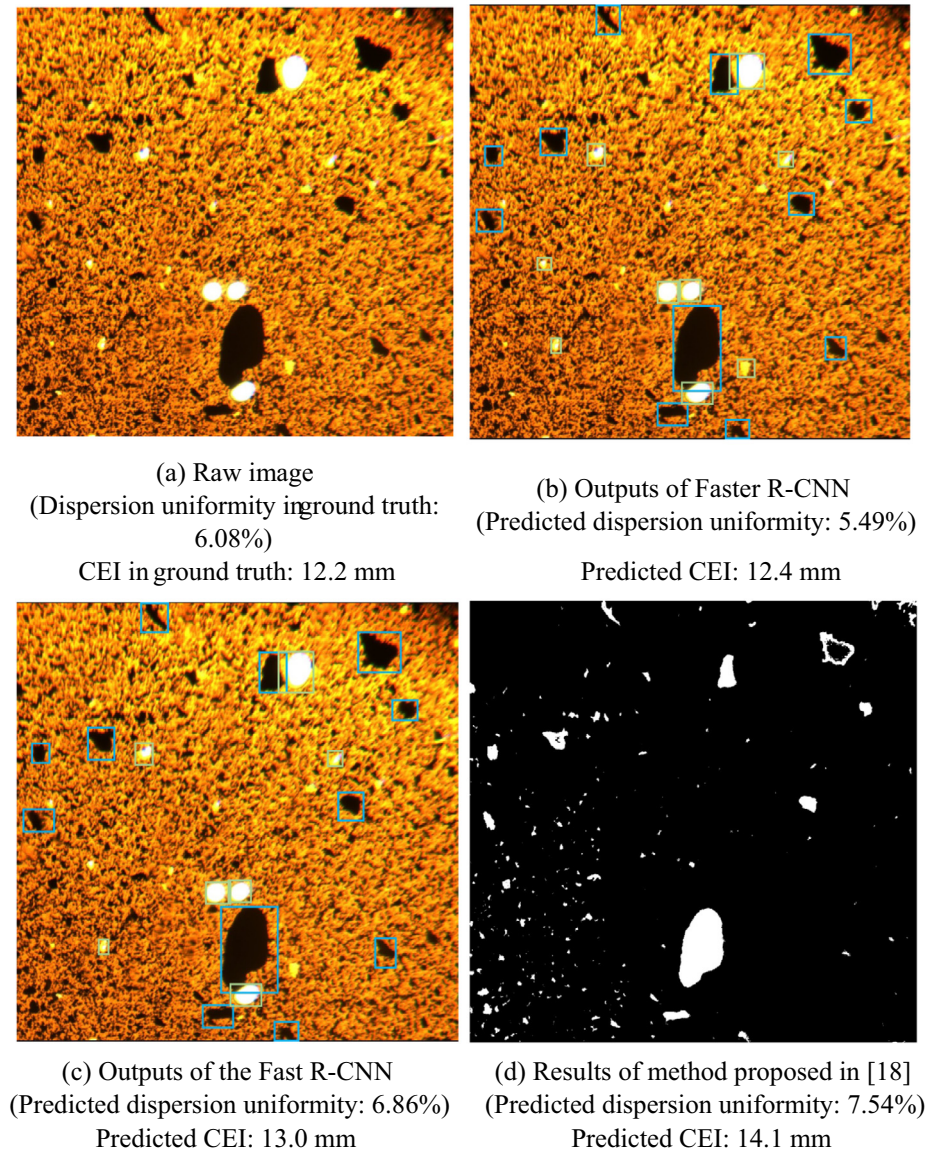
(a) Raw image
(Dispersion uniformity in ground truth: 6.08%)
CEI in ground truth: 12.2 mm

(b) Outputs of Faster R-CNN
(Predicted dispersion uniformity: 5.49%)
Predicted CEI: 12.4 mm

(c) Outputs of the Fast R-CNN
(Predicted dispersion uniformity: 6.86%)
Predicted CEI: 13.0 mm

(d) Results of method proposed in [18]
(Predicted dispersion uniformity: 7.54%)
Predicted CEI: 14.1 mm

Fig. 11. Example of comparative studies.

low-level color information and assembling complete high-level color information. As shown in Fig. 10(b) through (e), there are some bunches missing. These bunches concentrate on the dark areas, which are weak observation areas in an OP. Clearly, this problem can be solved by continuously moving the observation area. Therefore, the results in Fig. 10 also show the necessity to apply the Faster R-CNN in Case 16, not only in OP images but also in OP videos.

3.3. Comparative study

The proposed Faster R-CNN was compared with the traditional Fast R-CNN and the method proposed in [18] to show the superiorities in the location of graphite powder bunches and an evaluation of graphite powder dispersion in asphalt. Notably, the training set with data augmentation was also used to train the traditional Fast R-CNN. The detailed specifications of the Fast R-CNN are given in Table 4. A new OP image with a pixel resolution of 2048 × 2048 was taken using the method introduced in Section 2.1.2. The image, which included graphite powder bunches and lighting

spots, was cropped into four images with a pixel resolution of 1024 × 1024, and imported into the Faster R-CNN in Case 16 and the Fast R-CNN to test the precision. Additionally, the four cropped images were analyzed using the method proposed in [18].

The training time in GPU mode of the Faster R-CNN in Case 16 and the Fast R-CNN were approximately 6 and 40 h, respectively. The testing time required to evaluate an image with a pixel resolution of 1024 × 1024 in GPU mode was approximately 0.04 and 0.18 s for the two network types, respectively. Two records of the computation times showed that the Faster R-CNN was superior in terms of time, and provided a sufficient speed for quasi real-time detection. The average 0.04 s required to evaluate an image with a pixel resolution of 1024 × 1024 in GPU mode was acceptable for dealing with OP video, whereas 0.18 s was not reasonable.

The outputs of the Faster R-CNN and Fast R-CNN, and the results of the method proposed in [18], are shown in Fig. 11. As can be seen in Fig. 11, the Fast R-CNN also shows good results with high accuracy, as claimed in previous works in the field of deep learning [22,28]. Although the Faster R-CNN showed similar results, it provided more reasonable bounding boxes for the bunches and a
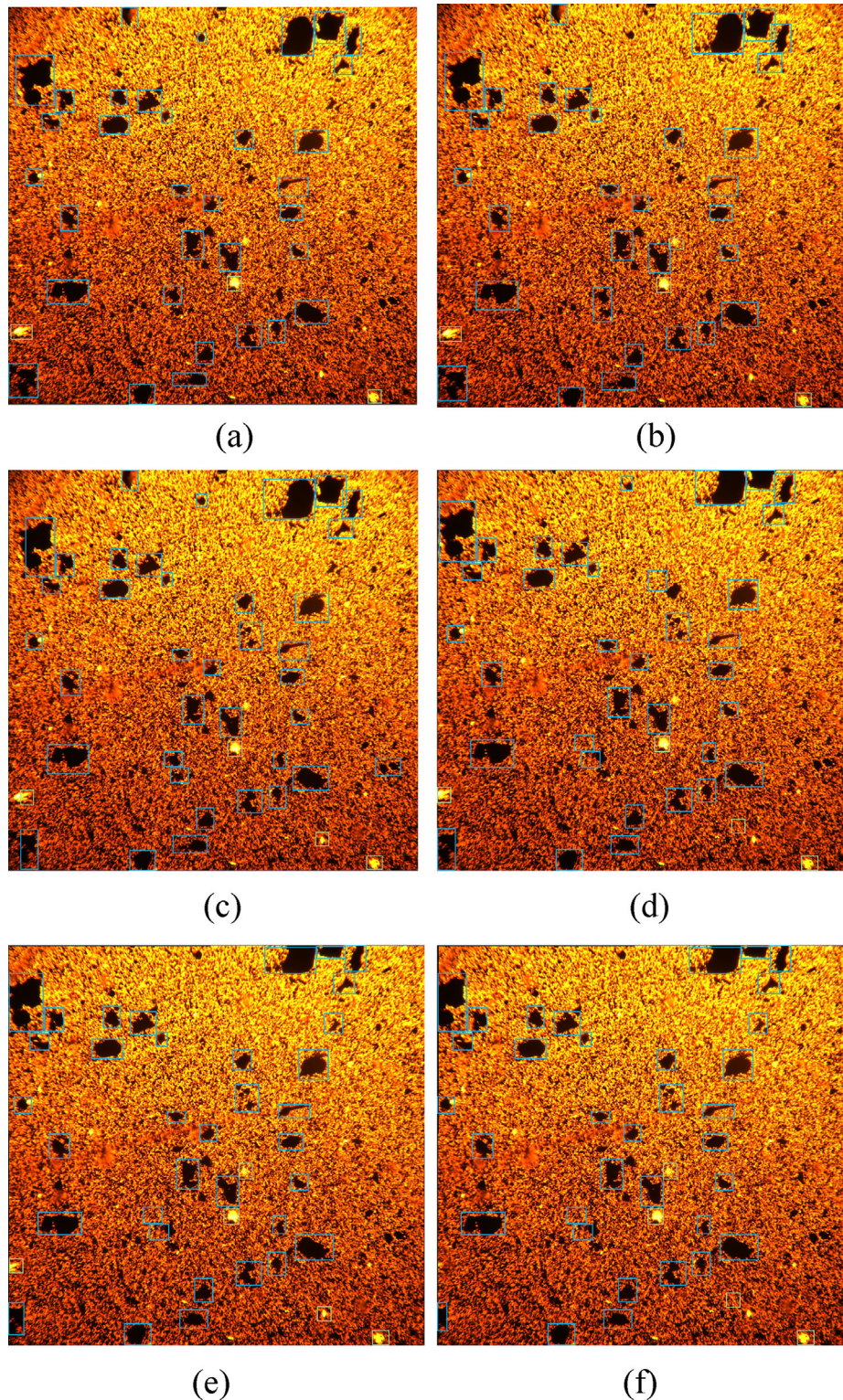
Fig. 12. Sample of six sequential frames from the provided OP video.

closer result of the dispersion uniformity and CEI. For example, the bounding box indicates precisely a large bunch in the bottom of the image in Fig. 11(b), whereas the bounding box for locating the same bunch in Fig. 11(c) includes some irrelevant information. Additionally, as shown in Fig. 11, the predicted CEI of the Faster R-CNN is 12.4 mm, which is closer to the true value compared with other two methods. This is because the sub-feature proposals pro-

vided by the RPN in the Faster R-CNN were more effective than the randomly selected sub-feature proposals in the Fast R-CNN. Additionally, nine anchors with different sizes and ratios in the Faster R-CNN had a better capacity to locate the bunches than the fixed sliding windows used in the Fast R-CNN.

As for the comparison between the Faster R-CNN and the method proposed in [18], the Faster R-CNN located each bunch

accurately, whereas the results of localization using the method proposed in [18] were unacceptable with some important information missing, particularly under poor lighting conditions.

4. Testing of videos

As shown in Fig. 1(g), the location and measurement was only based on a local examination, which could not reflect the entire dispersion uniformity of asphalt. To evaluate the entire scale distribution, a continuous observation and location should be realized. Additionally, a continuous inspection using OP video can solve the problem of incomplete bunches in OP images. Therefore, the location and measurement for the entire specimen should be realized using OP video based on the method using OP images.

The well-trained Faster R-CNN realized the evaluation of an image with a pixel resolution of 1024×1024 in GPU mode in approximately 0.04 s, which provided the possibility for a quasi-real-time evaluation using OP video. The testing speed indicated that the Faster R-CNN could evaluate OP videos with a pixel resolution of 2048×2048 at a frame rate of 6–8 fps, which was sufficient to evaluate graphite powder dispersion, even though it was insufficient for inspection objects in television and movie videos.

An OP video with a pixel resolution of 2048×2048 with a frame rate of 6 fps was used to test the well-trained Faster R-CNN. Fig. 12 shows a sample of six sequential frames from the provided OP video for an evaluation of graphite powder dispersion. As shown in Fig. 12, the method based the Faster R-CNN has the capacity of achieving a quasi-real-time autonomous dispersion evaluation in GPU mode, which can replace a human-assisted microcosmic dispersion evaluation based on static images with a computer-visual evaluation using OP videos.

5. Conclusions

The application of a Faster R-CNN by sharing a CNN between an RPN and a Fast R-CNN to locate graphite powder bunches and evaluate its dispersion using OP images and videos was presented in this paper, and the following conclusions can be drawn:

(1) The Faster R-CNN was used in Case 16, in which nine anchors had ratios of 0.3, 1.0, and 1.6 and sizes of 32, 128, and 192, achieving an average precision in locating the bunches of 91.2% and a dispersion uniformity of 84.0%. Its mean average precision was 87.5%. The Faster R-CNN used in Case 16 was considered the optimal one in this research.

(2) The training time in GPU mode of the Faster R-CNN in Case 16 was approximately 6 h, and the testing time used to evaluate an image with a pixel resolution of 1024×1024 in GPU mode was approximately 0.04 s. The results provided the possibility for a quasi-real-time evaluation using OP videos.

(3) Compared with the conventional Fast R-CNN, the Faster R-CNN provided more reasonable bounding boxes for bunches and a closer result of the dispersion uniformity. This was because the sub-feature proposals provided by the RPN in the Faster R-CNN were more effective than the randomly selected sub-feature proposals of the Fast R-CNN. In addition, nine anchors with different sizes and ratios in the Faster R-CNN had a better capacity to locate the bunches than fixed sliding windows in the Fast R-CNN.

(4) The method based on the Faster R-CNN had the capacity of a quasi-real-time autonomous dispersion evaluation in GPU mode. It can replace a human-assisted microcosmic dispersion evaluation based on static images using a computer-visual evaluation of OP videos.

Conflict of interest

The authors declared that they have no conflicts of interest to this work.

We declare that we do not have any commercial or associative interest that represents a conflict of interest in connection with the work submitted.

Acknowledgements

References

[1] Wu. Shaopeng, Pan Pan, Mingyu Chen, Analysis of characteristics of electrically conductive asphalt concrete prepared by multiplex conductive materials, J. Mater. Civ. Eng. 25 (7) (2017) 871–879.
[2] Hong Wang, Wu. Shaopeng, Mingyu Chen, Experimental research and simulating analysis of conductive asphalt concrete used to melting ice and snow, J. Wuhan Univ. Technol. 32 (7) (2010) 90–93.
[3] Zhenjun Wang, Ting Zhang, Liang Zhou, Investigation on electromagnetic and microwave absorption properties of copper slag-filled cement mortar, Cem. Concr. Compos. 74 (2016) 174–181.
[4] F. He, Graphite and expanded graphite, New Carbon Mater. 4 (1990) 12–19.
[5] Qili Wang, Hu. Yafei, Min He, Qi Liu, Fractal description of porosity and specific surface area for porous media of graphite, J. China Coal Soc. 35 (10) (2010) 1725–1729.
[6] Deyu Zhang, Xiaoming Huang, Ying Gao, Jinxiang Hong, Tao Bai, Effect of heterogeneity on greep behavior of asphalt concrete, J. Build. Mater. 16 (4) (2013) 614–620.
[7] L.C. Tang, Y.J. Wan, D. Yan, Y.B. Pei, L. Zhao, Y.B. Li, L.B. Wu, J.X.G.Q. Jiang, The effect of graphene dispersion on the mechanical properties of grapheme/epoxy composites, Carbon 60 (2013) 16–27.
[8] L.L. Chen, C. Xu, J. Liu, X.M. Fang, Z.G. Zhang, Optical absorption property and photo-thermal conversion performance of graphene oxide/water nanofluids with excellent dispersion stability, Sol. Energy 148 (2017) 17–24.
[9] Aihong Kang, Changjiang Kou, Xuanyu Liu, Evaluation methods of dispersed phase uniformity in SBS modified asphalt based on digital image analysis technology, J. Sichuan Univ. (Eng. Sci. Ed.) 46 (1) (2014) 172–176.
[10] Lv Fang, Shufen Li, Measurement of dimension of carbon black particles in rubber by mathematical morphology, Phys. Test. Chem. Anal. 44 (12) (2008) 689–693.
[11] L.Y. Woo, S. Wansom, N. Ozyurt, B. Mu, S.P. Shah, T.O. Mason, Characterizing fiber dispersion in cement composites using AC-impedance spectroscopy, Cem. Concr. Compos. 27 (6) (2005) 627–636.
[12] Zhenjun Wang, Wu. Jiayu, Peng Zhao, Nan Dai, Zhiwei Zhai, Tao Ai, Improving cracking resistance of cement mortar by thermo-sensitive poly N-isopropyl acrylamide (PNIPAM) gels, J. Cleaner Prod. 176 (2018) 1292–1303.
[13] Y. Xiao, G.L. Zheng, Quality control of SBS modified asphalt based on micro-disperse state analysis, J. Highway Transp. Res. Dev. 22 (12) (2005) 17–19.
[14] H. Yao, L. Li, X.L. Yang, H.C. Dan, S.P. Luo, Mechanics performance research and microstructure analysis of nanomaterials modified asphalt, J. Build. Mater. 14 (5) (2011) 712–717.
[15] Jie Gao, Zhenjun Wang, Ting Zhang, Zhou Liang, Dispersion of carbon fibers in cement-based composites with different mixing methods, Constr. Build. Mater. 134 (2017) 220–227.
[16] J. Huang, Z.B. Hao, W. Zou, K.J. Wang, W. Cheng, Effects of carbonization pressure on microstructure of graphitized pitch-derived carbons, J. Inorg. Mater. 25 (3) (2010) 321–326.
[17] F. Shen, M.Y. Zhao, J. Lu, L.G. Qiao, K. Guo, Q.J. Ding, The research of diffusion mechanism of modified regenerant in aging asphalt, J. Funct. Mater. 21 (45) (2014) 21064–21067.
[18] Z.J. Wang, J. Gao, T. Ai, W. Jiang, P. Zhao, Quantitative evaluation of carbon fiber dispersion in cement based composites, Constr. Build. Mater. 68 (2014) 26–30.
[19] Y. LeCun, Generalization and network design strategies, in: Connections in Perspective, North-Holland, Amsterdam, 1989, pp. 143–155.
[20] Y. LeCun, Y. Bengio, Convolutional networks for images, speech, and time series, in: The Hand Book of Brain Theory and Neural Networks, MITPress, 1995, p. 3361.

[21] Biao Leng, Shuang Guo, Xiangyang Zhang, Zhang Xiong, 3D object retrieval with stacked local convolutional autoencoder, Signal Process. 112 (2015) 119–128.

[22] Xu. Jun, Xiaofei Luo, Guanhao Wang, Hannah Gilmore, Anant Madabhushi, A deep convolutional neural network for segmenting and classifying epithelial and stromal regions in histopathological images, Neurocomputing 191 (2016) 214–223.

[23] Zheng Tong, Jie Gao, Zhenqiang Han, Zhenjun Wang, Recognition of asphalt pavement crack length using deep convolutional neural networks, Road Mater. Pavement Des. (Published online).

[24] Zheng Tong, Jie Gao, Zhang Haitai, Innovation for evaluating aggregate angularity based upon 3D convolutional neural network, Constr. Build. Mater. 155 (2017) 919–929.

[25] Zheng Tong, Jie Gao, Haitao Zhang, Recognition, location, measurement and 3D reconstruction of concealed cracks using convolutional neural networks, Constr. Build. Mater. 146 (2017) 775–787.

[26] Zheng Tong, Aimin Sha, Jie Gao, Innovation for recognizing pavement disease using convolutional neural network, 2017 World Transport Convention, Beijing, China, June 4–6, 2017.

[27] Zheng Tong, Jie Gao, Haitao Zhang, Innovative method for recognizing subgrade defects based on a convolutional neural network, Constr. Build. Mater. 169 (2018) 69–82.

[28] Y.J. Cha, W. Choi, G. Suh, S.M ahmoudkhani, O. Büyüköztürk, Autonomous structural visual inspection using region-based deep learning for detecting multiple damage types, Comput.-Aided Civ. Infrastruct. Eng.. (Published online)

[29] Y.J. Cha, W. Choi, O. Büyüköztürk, Deep learning-based crack damage detection using convolutional neural networks, Comput.-Aided Civ. Infrastruct. Eng. 32 (5) (2017) 361–378.

[30] Y.Z. Lin, Z.H. Nie, H.W. Ma, Structural damage detection with automatic feature-extraction through deep learning, Comput.-Aided Civ. Infrastruct. Eng. (Published online).

[31] T.Y. Liao, On-line vehicle routing problems for carbon emissions reduction, Comput.-Aided Civ. Infrastruct. Eng. (Published online).

[32] M. Koziarski, B. Cyganek, Image recognition with deep neural networks in presence of noise-dealing with and taking advantage of distortions, Integr. Comput.-Aided Eng. 24 (4) (2017) 337–350.

[33] F. Ortega-Zamorano, J.M. Jerez, I. Gómez, L. Franco, Layer multiplexing FPGA implementation for deep back-propagation learning, Integr. Comput.-Aided Eng. 24 (2017) 171–185.

[34] M.H. Rafiei, W.H. Khushefati, R. Demirboga, H. Adeli, Supervised deep restricted boltzmann machine for estimation of concrete compressive strength, ACI Mater. J. 114 (2) (2017) 237–244.

[35] M.H. Rafiei, H. Adeli, A novel machine learning based algorithm to detect damage in highrise building structures, Struct. Des. Tall Special Build. 26 (2017) 18 (10.1002/tal.1400).

[36] J.Y. Yu, X.F. Luo, S.P. Wu, X. Zeng, P.L. Cong, Preparation and properties of flame-retarded SBS modified asphalt, China J. Highway Transp. 20 (2) (2007) 35–39.

[37] L. Sun, H.R. Zhu, X.T. Xin, H.Y. Wang, W.J. Gu, Preparation of nano-modified asphalt and its road performance evaluation, China J. Highway Transp. 26 (1) (2013) 15–22.

[38] F.Q. Dong, Y.Z. Zhang, X. Xin, W.Y. Fan, G.Z. Nan, Preparation and microstructure of composite modified hard asphalt, J. China Univ. Pet. 38 (4) (2014) 174–179.

[39] C.X. Qian, J.G. Xie, H.B. Wang, Preparation and properties of grafting SBS modified asphalt, J. Southeast Univ. (Nat. Sci. Ed.) 35 (3) (2005) 404–408.

[40] M. Wang, L.P. Liu, Investigation of the microscopic phase of SBS modified bitumen with fluorescence microscope (FM), J. Transport Sci. Eng. 30 (3) (2014) 10–14.

[41] Wang Zhenjun, Wang Qiong, Ai Tao, Comparative study on effects of binders and curing ages on properties of cement emulsified asphalt mixture using gray correlation entropy analysis, Constr. Build. Mater. 54 (2014) 615–622.

[42] A.H. Kang, W.H. Zhang, L.J. Sun, Preparation method of modified asphalt fluorescence optical microscopy sample, J. Sichuan Univ. (Eng. Sci. Ed.) 44 (2) (2012) 154–158.

[43] R. Girshick, Fast R-CNN, in: Proceedings of the IEEE International Conference on Computer Vision, Santiago, Chile, 07–13 December, 2015, pp. 1440–1448.

[44] V. Nair, G.E. Hinton, Rectified linear units improve restricted Boltzmann machines, in: Proceedings of the 27th International Conference on Machine Learning (ICML-10), Haifa, Israel, 21–24 June 2010, pp. 807–814.

[45] S. Ren, K. He, R. Girshick, J. Sun, Faster R-CNN: towards real-time object detection with region proposal networks, IEEE Trans. Pattern Anal. Mach. Intell. 39 (6) (2016) 1137–1149.

[46] Erfanifard Yousef, Saborowski Joachim, Wiegand Kerstin, M. Meyer Katrin, Efficiency of sample-based indices for spatial pattern recognition of wild pistachio (Pistacia atlantica) trees in semi-arid woodlands, J. For. Res. 27 (3) (2016) 583–594.

[47] K. He, X. Zhang, S. Ren, J. Sun, Spatial pyramid pooling in deep convolutional networks for visual recognition, in: Proceeding of the 13th European Conference on Computer Vision, Zurich, Switzerland, 6–12 September 2014, pp. 346–361.